Arctic Sea Ice Growth in Response to Synoptic- and Large-Scale Atmospheric Forcing from CMIP5 Models

LEI CAI

NORCE Norwegian Research Centre, and Bjerknes Centre for Climate Research, Bergen, Norway

VLADIMIR A. ALEXEEV AND JOHN E. WALSH

International Arctic Research Center, University of Alaska Fairbanks, Fairbanks, Alaska

(Manuscript received 5 May 2019, in final form 15 April 2020)

ABSTRACT

We explore the response of wintertime Arctic sea ice growth to strong cyclones and to large-scale circulation patterns on the daily scale using Earth system model output in phase 5 of the Coupled Model Intercomparison Project (CMIP5). A combined metrics ranking method selects three CMIP5 models that are successful in reproducing the wintertime Arctic dipole (AD) pattern. A cyclone identification method is applied to select strong cyclones in two subregions in the North Atlantic to examine their different impacts on sea ice growth. The total change of sea ice growth rate (SGR) is split into those respectively driven by the dynamic and thermodynamic atmospheric forcing. Three models reproduce the downward longwave radiation anomalies that generally match thermodynamic SGR anomalies in response to both strong cyclones and large-scale circulation patterns. For large-scale circulation patterns, the negative AD outweighs the positive Arctic Oscillation in thermodynamically inhibiting SGR in both impact area and magnitude. Despite the disagreement on the spatial distribution, the three CMIP5 models agree on the weaker response of dynamic SGR than thermodynamic SGR. As the Arctic warms, the thinner sea ice results in more ice production and smaller spatial heterogeneity of thickness, dampening the SGR response to the dynamic forcing. The higher temperature increases the specific heat of sea ice, thus dampening the SGR response to the thermodynamic forcing. In this way, the atmospheric forcing is projected to contribute less to change daily SGR in the future climate.

1. Introduction

Arctic sea ice has become thinner and "younger" (Wadhams and Davis 2000; Maslanik et al. 2007; Serreze and Stroeve 2015). Submarine observations have shown a thinning trend of Arctic sea ice since 1958 (Kwok and Rothrock 2009). The observed fraction of multiyear ice in March has decreased from 61% in 1984 to about 34% in 2018 (NSIDC 2018). A reconstruction based on multisource observations estimates a 65% reduction of annual mean sea ice thickness from 1975 to 2012 (Lindsay and Schweiger 2015). Younger and thinner sea ice melts faster than the multiyear ice during the summer months (Maykut 1978; Tschudi et al. 2016), which could play a role in the recent large decrease of Arctic sea ice extent in September (Stroeve et al. 2008; Yang and Magnusdottir 2017). Multimodel projections indicate a median timeline of the 2030s when the Arctic Ocean begins to be ice-free in the summer (Wang and Overland 2012).

Previous studies have acknowledged the significance of wind forcing in influencing wintertime sea ice growth. The frequent cyclone activity near Iceland forms a semipermanent Icelandic low as a part of North Atlantic Oscillation–Arctic Oscillation (NAO-AO) variability (Serreze and Barry 1988; Serreze et al. 1997). The NAO-AO is an annular pattern of sea level pressure (PSL) anomaly and is the dominant mode of wintertime climate variability in the Arctic (Thompson and Wallace

Denotes content that is immediately available upon publication as open access.

Supplemental information related to this paper is available at the Journals Online website: https://doi.org/10.1175/JCLI-D-19-0326.s1.

Corresponding author: Lei Cai, leca@norceresearch.no

DOI: 10.1175/JCLI-D-19-0326.1

1998). Corresponding to lower PSL over the Arctic, a positive NAO-AO in winter drives a stronger counterclockwise motion of sea ice, shrinking its area and leaving more space along the Arctic coast for fresh sea ice to grow (Deser 2000; Rigor et al. 2002). The young and thin coastal sea ice typically melts out the following summer, resulting in a substantial Arctic sea ice retreat (Serreze et al. 2007b). For winters with a positive AO, a numerical model with data assimilation simulates a reduction of sea ice thickness by 10–15 cm by the end of March in the Eurasian and Pacific sector of the Arctic Ocean (Park et al. 2018).

While verifying the importance of wind forcing on seasonal-scale sea ice growth, Bitz et al. (2002) suggested that sea ice behavior is not sensitive to daily wind variability. Meanwhile, the poleward moisture and heat transports through the North Atlantic could enhance downward longwave radiation and surface warming in the Arctic, becoming a thermodynamic forcing that could inhibit sea ice growth (Serreze et al. 2007a; Woods et al. 2013). Woods and Caballero (2016) found that the increasing number of wintertime moisture intrusion events through the Atlantic since 2000 could contribute to as much as a 35% decrease in wintertime sea ice concentration in the Barents Sea due to the regional enhancement of downward longwave radiation flux. A numerical simulation of the life cycle of a moisture intrusion event showed that the thermodynamic forcing by enhanced downward longwave radiation flux outweighs the effect of wind-driven ice drift in inhibiting sea ice growth after the first couple of days and that the downward longwave radiation was the dominant forcing for as long as 1–2 weeks (Park et al. 2015). Alexeev et al. (2017) suggested that strong Atlantic cyclones accompanied by the negative phase of the Arctic dipole (AD) favor the transport of warm and moist air into the central Arctic. Since poleward airflow affects sea ice both dynamically (through surface wind stress) and thermodynamically (by the advection of atmospheric moisture and heat), it is worth exploring the relative importance of the dynamic and thermodynamic forcings of sea ice growth on time scales of days in the context of the broader atmospheric circulation.

Nordic cyclones occur over both the Icelandic low area and the Norwegian and Barents Seas during winter (Rogers 1997; Gulev et al. 2001; Zhang et al. 2004). Depending on their location, these cyclones can produce the atmospheric forcing in distinctively different manners. Thermodynamically, cyclones in the Norwegian and Barents Seas are associated with near-surface temperature increases over western Siberia and the Arctic coast to its north (Boisvert et al. 2016). Dynamically, these cyclones bring northerly wind over the Fram Strait, favoring sea ice advection toward the warmer Atlantic water (Tsukernik et al. 2010; Wei et al. 2019). With respect to large-scale circulation patterns, the dynamic and thermodynamic forcing from cyclones over the Norwegian and Barents Seas resembles that of the positive AO (Park et al. 2018). Park et al. (2018) suggested that the AO drives the stronger dynamic than thermodynamic sea ice thickness change on the seasonal scale. For this reason, we compare daily sea ice growth response to cyclones in different regions (Icelandic low region vs Norwegian and Barents Seas) and to different large-scale atmospheric circulation patterns (negative AD vs positive AO).

While addressing our research question requires daily averaged sea ice data, there have not been any routine daily observations of sea ice thickness over the whole Arctic. Therefore, we chose to apply the output from the latest generation of Earth system models in phase 5 of the Coupled Model Intercomparison Project (CMIP5; Taylor et al. 2012) to explore ice–atmosphere interactions. Although previous studies suggested that CMIP5 models diverge from each other and observations in simulating the trend and variability of sea ice thickness, the trajectory of summer sea ice in recent years has come into closer alignment with model projections (Stroeve et al. 2012, 2014). Moreover, the models' fully coupled framework guarantees the physically consistent interaction between the atmosphere, ocean, and sea ice that is essential for this study.

Finally, the projections in the twenty-first century make it possible for us to explore how sea ice–atmosphere interaction would evolve in the future climate. As a warmer Arctic in the future implies a thinner sea ice cover, a change in the short-term response of sea ice to the atmospheric forcing becomes a distinct possibility and is investigated here. With regard to cyclone activity, previous CMIP5 model-based studies suggest that cyclone activity in the Nordic seas weakens slightly in both intensity and frequency in the twenty-first century compared to the twentieth century (Mizuta 2012; Zappa et al. 2013). The present study aims to explore the daily scale relationship between wintertime strong Nordic seas cyclones, large-scale climatic variability, and sea ice growth in multiple CMIP5 models covering both the past and future climate. This study addresses the following research questions:

1) Do CMIP5 models agree with each other on the response of wintertime central Arctic sea ice growth to strong cyclones and large-scale circulation patterns on a daily scale?
2) Given the dynamic and thermodynamic forcing of sea ice by the atmosphere, do either dominate in affecting daily sea ice growth?

3) How and why does the response of daily-scale sea ice growth to both the thermodynamic and dynamic forcings change with a warmer Arctic and thinner sea ice cover in the twenty-first century?

2. Methodology

a. CMIP5 model selection

We choose to select a subset of CMIP5 models for further analyses based on how successful they are in reproducing the AD pattern. It is because the surface wind pattern associated with moisture intrusions into the Arctic resembles that associated with the negative phase of AD (Park et al. 2015; Alexeev et al. 2017; Woods et al. 2017). Furthermore, a large-scale blocking pattern over Eurasia that resembles the negative AD pattern has been suggested to play an important role in deflecting cyclones and the associated moisture into the Arctic for strong moisture intrusions originated from both the North Atlantic and the Barents–Kara Seas (Woods et al. 2013; Gong and Luo 2017). We calculate the winter AD through the empirical orthogonal function (EOF) analysis on the December–February (DJF) sea level pressure using the first ensemble member of 30 CMIP5 models in the historical period (1950–2005). The dipole-shaped pattern of the AD appears in the second to fifth EOF mode in the 30 models. We rank models using a combined-metrics approach with the NCEP–NCAR reanalysis (Kistler et al. 2001) as a reference dataset, which has been proven successful in ranking CMIP5 models in producing climate variability modes (Cai et al. 2018). The full ranking and more details including combined-metrics scores and the winter AD patterns are available in the online supplemental material. Unlike in Cai et al. (2018), the combined-metrics ranking in this study does not involve the AO as most CMIP5 models are fairly successful in reproducing the wintertime AO pattern According to the evaluation result by the Climate Variability Diagnostics Package (CVDP; http://www.cesm.ucar.edu/working_groups/CVC/cvdp) of the Community Earth System Model working group (Phillips et al. 2014).

Data availability is the other prerequisite of our model selection. For the top 25% (top 7) of the 30 models, CSIRO-Mk3.6.0, HadGEM2-AO, HadGEM2-CC, and MRI-CGCM3 miss some necessary variables in the database of Earth System Grid Federation (ESGF; http://esgf-node.llnl.gov/projects/esgf-llnl). We, therefore, select the remaining three models (ACCESS1.3, MIROC5, and MPI-ESM-LR) for further analyses. The climate variables of interest include sea level pressure (PSL), downwelling longwave radiation at the surface (DLW), and surface wind from the atmosphere component, as well as the concentration, thickness, and velocity of sea ice from the sea ice component. For the future projection, we select the model output for the period of 2006–50 under the RCP8.5 scenario.

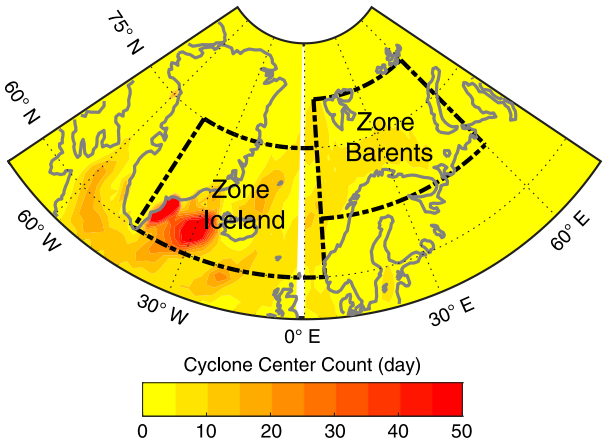

FIG. 1. Three-model (ACCESS1.3, MIROC5, and MPI-ESM-LR) ensemble of cyclone center counts (contours) during the winter months (November–March) in the historical period (1950–2005). The black dash–dotted lines delimit Zone Iceland and Zone Barents, in which the storm identification approach is applied.

b. Cyclone identification

We employ a cyclone identification method that originates from Serreze et al. (1997) to search for days with strong cyclone activity from November to March (NDJFM). Candidates for cyclone centers need to meet the following criteria: 1) the grid point has a PSL lower than all eight surrounding grid points, and 2) the pressure gradient from the grid point to its surrounding points is higher than 2 hPa $(100\,\text{km})^{-1}$. Two (or more) cyclone center candidates merge as one single cyclone if they are closer than 1200 km from each other. The cyclone center, in this case, is located at the cyclone center with the lowest PSL. We take the difference between PSL at the cyclone center and the monthly climatology of PSL for the same grid point as the cyclone intensity. We select the cyclones with the top 10% of intensities as the strong cyclones.

We conduct the cyclone identification in two separate zones, as cyclones in different regions of the Nordic seas are hypothesized to have different impacts on the central Arctic (Fig. 1). Zone Iceland covers the coastal area to the southeast of Greenland, the western Norwegian Sea, and the southern Greenland Sea. Zone Barents is to the northeast of Zone Iceland, covering most of the Norwegian and Barents Seas. This categorization is based on the statistics of winter cyclones in the North Atlantic by Zhang et al. (2004), who show distinct clusters of cyclone centers to the southeast of Greenland and off the northwest coast of Norway. For the three chosen models, the majority of cyclones are located in

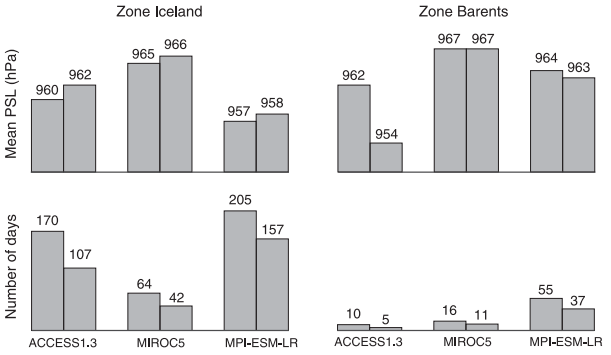

FIG. 2. The statistics for days with strong (top 10%) cyclones and the mean PSL at cyclone center in both zones. For each set of bars, the left bar is for the historical period (1950–2005), and the right bar is for the projected period (2006–50).

Zone Iceland, although there are also substantial numbers of cyclones in Zone Barents (Fig. 1). The spatial distribution of the models' cyclone centers is generally similar to that in observation and reanalysis datasets (Zhang et al. 2004; Rudeva and Gulev 2011). We exclude Greenland from cyclone identification, as its high altitude could bring low pressure biases when extrapolating surface pressure to sea level.

Note that the above cyclone identification screens out days with a strong cyclonic circulation pattern rather than the whole life cycle or trajectory of strong cyclone events (Fig. 2). In the selected days with a strong cyclonic circulation, the cyclone usually reaches its maximal intensity. Some cyclone events may have more than one day counted throughout their life cycle as they retain their strength (top 10% in intensity). Both zone counts may also include the same cyclone event if it forms in Zone Iceland and moves into Zone Barents later while maintaining high intensity. Although there are some disagreements on the frequency and intensity of strong cyclones between models, the three models agree that the number of strong cyclones decreases in the RCP8.5 in both zones, while the intensity of cyclones shows little change. The distinct increase in cyclones' intensity for ACCESS1.3 in Zone Barents is not significant as there are few strong cyclones in this case (Fig. 2).

c. *Daily indices of AO and AD and sea ice growth response*

This study calculates the daily indices of AO and AD as the regression coefficient between the anomaly patterns of the PSL and the winter AO and AD. The patterns of AO and AD are calculated using the data from each selected model's historical period (1950–2005) product. Note that the AO and AD patterns for each model vary slightly from each other, although all the patterns are close to those in the reanalysis data because these models rank in the top several for their success in reproducing the patterns AO and AD. (The AD patterns are shown in the supplemental material, while the AO patterns can be obtained via http://www.cesm.ucar.edu/working_groups/CVC/cvdp.) Using the historical AO and AD patterns to calculate the indices of AO and AD in both the historical and projected periods guarantees that the calculated index is consistently associated with the same PSL anomaly pattern. The Climate Prediction Center of the National Weather Service has been using a similar method to update the daily AO index (http://www.cpc.ncep.noaa.gov/products/precip/CWlink/daily_ao_index/ao.shtml).

We define the total sea ice growth rate (SGR) as the local derivative of sea ice thickness with respect to time. We calculate the SGR due to ice drift as the ice flux divergence:

$$\frac{\Delta h}{\Delta t} = -\left[\frac{\partial(uh)}{\partial x} + \frac{\partial(vh)}{\partial y}\right], \tag{1}$$

in which u and v are the sea ice velocity components, and h is the gridcell mean sea ice thickness. Integrating the ice flux divergence for 1 day (86 400 s) gives the daily dynamic SGR, which can be positive or negative. We estimate the thermodynamic SGR as the difference between the total and dynamic SGRs. We exclude all grid points in which the sea ice concentration is less than 90% or the sea ice thickness less than 0.1 m from analyses. A larger fraction of open water in a grid cell could interfere with the interaction between sea ice and atmosphere. An overly thin sea ice body in a grid cell may occur because of decreases of not only SGR but also sea ice concentration in response to the atmospheric forcing. These grid cells are therefore more likely to show inconsistencies of SGR response. We directly apply the average sea ice thickness in the CMIP5 model output, which is the average thickness for the whole grid including the ice-free part. Removing grid points with less than 90% sea ice concentration makes the difference between the average sea ice thickness and physical sea ice thickness fairly small.

The RCP8.5 scenario projects the most rapid warming of climate among all RCP scenarios, especially for the Arctic. It is also the scenario that is most consistent with the recent (post-2005) trajectory of greenhouse gas increases. We use a 21-yr moving average (10 years before and 10 years after) of climatic variables for each calendar day, providing the daily climatology to calculate anomalies. For example, we calculate the daily anomaly in 2000 based on the daily climatology calculated from 1990 to 2010. Our chosen periods (1950–2005 and 2006–50) in this way require the data from 1940 to 2060. As this study explores the wintertime sea ice growth, solar radiation and turbulent heat fluxes are expected to be

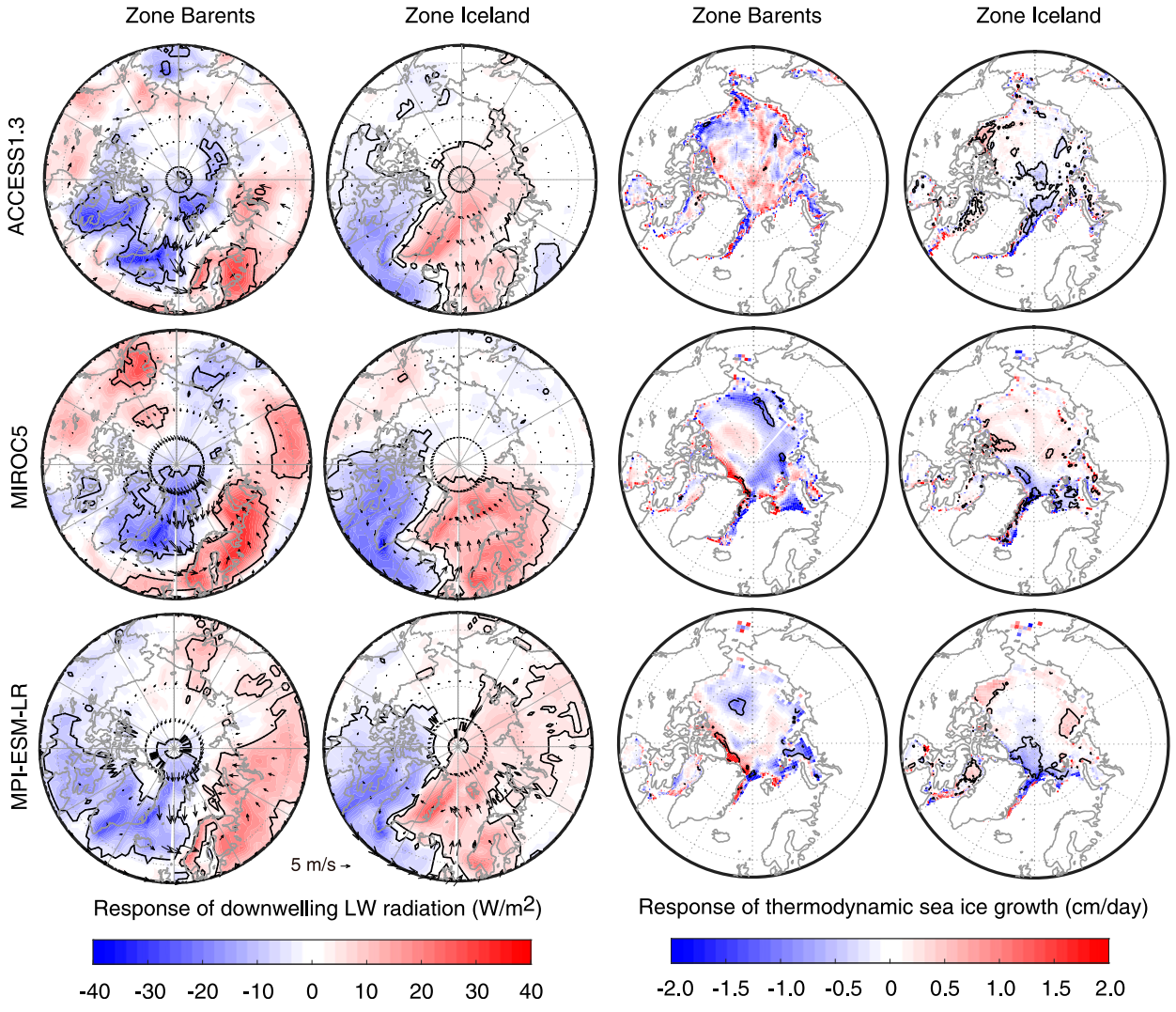

FIG. 3. (left) Anomalies of daily downwelling longwave radiation at the surface ($W\,m^{-2}$; shaded) and wind (vectors) in the response of the strong cyclones in Zone Barents and Zone Iceland in the three chosen models in the historical period (1950–2005). (right) Anomalies of thermodynamic SGR (cm day^{-1}; shaded) in response to the strong cyclones in Zone Barents and Zone Iceland in the historical period (1950–2005). Black solid lines delimit the regions in which the anomaly passes the *t* test with a 95% significance level.

negligibly low for the Arctic (Serreze et al. 2007a). We, therefore, use the DLW to approximate the thermodynamic forcing from the atmosphere as in other previous studies (e.g., Park et al. 2015; Woods and Caballero 2016). We include the analysis of other energy fluxes, as well as the residual of the surface energy budget, in the supplemental material to prove the dominant effect of the DLW in this study.

3. Results

a. Sea ice growth response to strong storms

For strong cyclones in Zone Iceland, the composite analysis in the historical period shows the southerly anomalous wind blowing from the North Atlantic to the central Arctic, along with the positive DLW anomalies (5–20 $W\,m^{-2}$) over the North Atlantic, the Barents Sea, and the Greenland Sea (Fig. 3). The northerly wind anomaly over the Atlantic for strong cyclones in Zone Barents is opposite in wind direction to that associated with strong cyclones in Zone Iceland. Correspondingly, the anomalous wind in the Zone Barents cyclones is associated with a different DLW pattern compared to strong cyclones in Zone Iceland, for which there are negative DLW anomalies over the Greenland Sea and part of the central Arctic and positive anomalies over Scandinavia and Siberia. In addition, the anomalous wind over Scandinavia blows eastward from the Atlantic

Ocean to eastern Europe. Considering that the Atlantic water surface is warmer than the ambient land during winter, such anomalous wind transports heat and moisture and leads to positive DLW anomalies over eastern Europe and Siberia, as well as some coastal regions in the Arctic Ocean. The magnitude of the DLW anomaly (5–20 $W m^{-2}$) is comparable to that from the strong cyclones in Zone Iceland.

The spatial distributions of the daily thermodynamic SGR anomaly generally match those of DLW in response to strong cyclones in Zone Iceland (Fig. 3). The greatest thermodynamic SGR inhibition (up to 2 $cm day^{-1}$) is in the Greenland and Barents Seas, extending to the central Arctic. For the strong cyclones in Zone Barents, the thermodynamic SGR inhibition with similar intensity (up to 2 $cm day^{-1}$) is in the Laptev and East Siberian Seas for MIROC5, and in the Greenland Sea and the Beaufort Sea for MPI-ESM-LR. In ACCESS1.3 and MIROC5, the thermodynamic SGR patterns for Zone Barents cyclones do not spatially match the DLW pattern. The small sample sizes of strong cyclonic days in these two models are partially responsible for these differences (Fig. 2), considering that most thermodynamic SGR inhibition in these cases is not statistically significant. The calculation of ice flux divergence could be inaccurate near the ice edge because of the discontinuity of the gridded ice concentrations, causing biases to the calculation of dynamic and thermodynamic SGRs. The biases cause the noisy signal along the coast and the ice edge on the Atlantic side. (See figures for the total SGR in the online supplemental material.)

The projections under the RCP8.5 scenario show a warmer Arctic with thinner and smaller sea ice coverage. Over the polar cap (80°N poleward), the abrupt decrease of wintertime sea ice (NDJFM) thickness starts around the 1990s in all three models (Fig. 4a). The sea ice cover by 2050 is about 1.5 m thinner on average compared to that in the 1990s. Meanwhile, DLW over the polar cap increases at the rate of 2–3 $W m^{-2}$ $decade^{-1}$ (Fig. 4b). The mean sea ice area in the Atlantic sector of the Arctic Ocean (60°E–60°W) decreases, while the mean SST over the open-water area in the North Atlantic (poleward of 60°N) increases (Figs. 4c,d). We detrend the time series in order to filter out the long-term trend (global warming) and to emphasize interannual variability before calculating the linear correlations. The linear correlation coefficients for the detrended time series are negative between DLW and sea ice area, and positive between DLW and SST (Table 1). All linear correlations have at least a 93% significance level. The statistical significance of the correlations suggests that a larger open-water area with a warmer sea surface corresponds strongly with the DLW increase in the central Arctic.

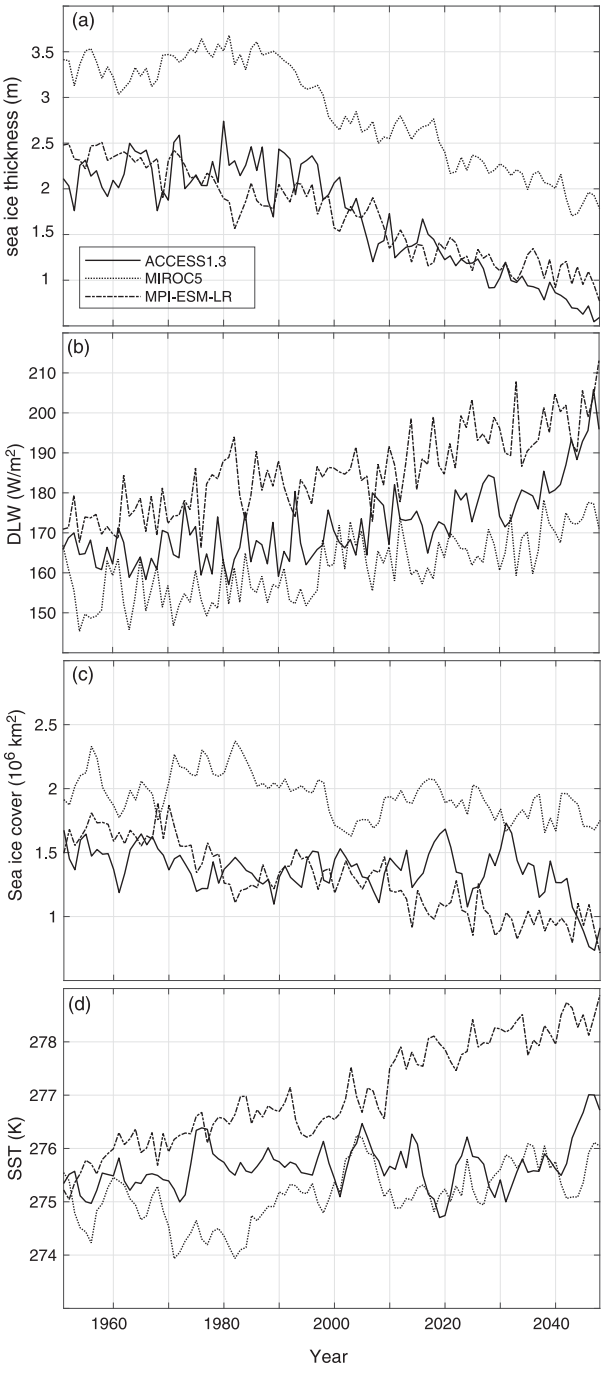

FIG. 4. The time series of (a) sea ice thickness and (b) DLW averaged over the polar cap (80°–90°N), and of (c) the area with sea ice cover and (d) SST over the open water averaged over the Atlantic sector of the Arctic Ocean (66°–90°N, 30°E–60°W), from November to March in the years of 1950–2050 for the three chosen models.

In the projection period, the composite analysis in terms of strong cyclones shows similar DLW anomaly

TABLE 1. The correlation coefficients and the p values between the time series of DLW over the polar cap (in Fig. 4b; detrended) and of the sea ice cover (in Fig. 4c; detrended) and open-water sea surface temperature (in Fig. 4d; detrended) over the Atlantic sector of the Arctic Ocean.

Correlation to DLW (detrended)	ρ_{sic}	p value	ρ_{SST}	p value
ACCESS1.3	−0.53	<0.1%	0.31	0.2%
MIROC5	−0.42	<0.1%	0.31	0.2%
MPI-ESM-LR	−0.48	<0.1%	0.18	7%

patterns when compared to the historical period (Fig. 5), while the impact area shrinks slightly for all three models. The statistics in the RCP8.5 period show slight decreases in both the frequency and intensity of strong cyclones in Zone Iceland, while strong cyclones in Zone Barents increase slightly in intensity in ACCESS1.3 and MPI-ESM-LR (Fig. 2). Correspondingly, the positive DLW anomaly becomes greater in magnitude in ACCESS1.3 (over 20 W m^{-2} higher) and MPI-ESM-LR (about 5 W m^{-2} higher) over western Siberia, whereas the small sample size (5 days with strong cyclonic circulation) for ACCESS1.3 weakens the significance. The thermodynamic SGR responses in the RCP8.5 period show similar patterns compared to those in the historical period, while both the magnitude of the anomaly and the impact area decrease noticeably for all three models.

The response of dynamic SGR to strong cyclones has a similar impact area to that of thermodynamic SGR (Fig. 6). Among the three models, the anomalies of dynamic and thermodynamic SGRs are of the same sign in ACCESS1.3, meaning inhibition of dynamic SGR coincides spatially with inhibition of thermodynamic SGR. On the contrary, the dynamic SGR response has the

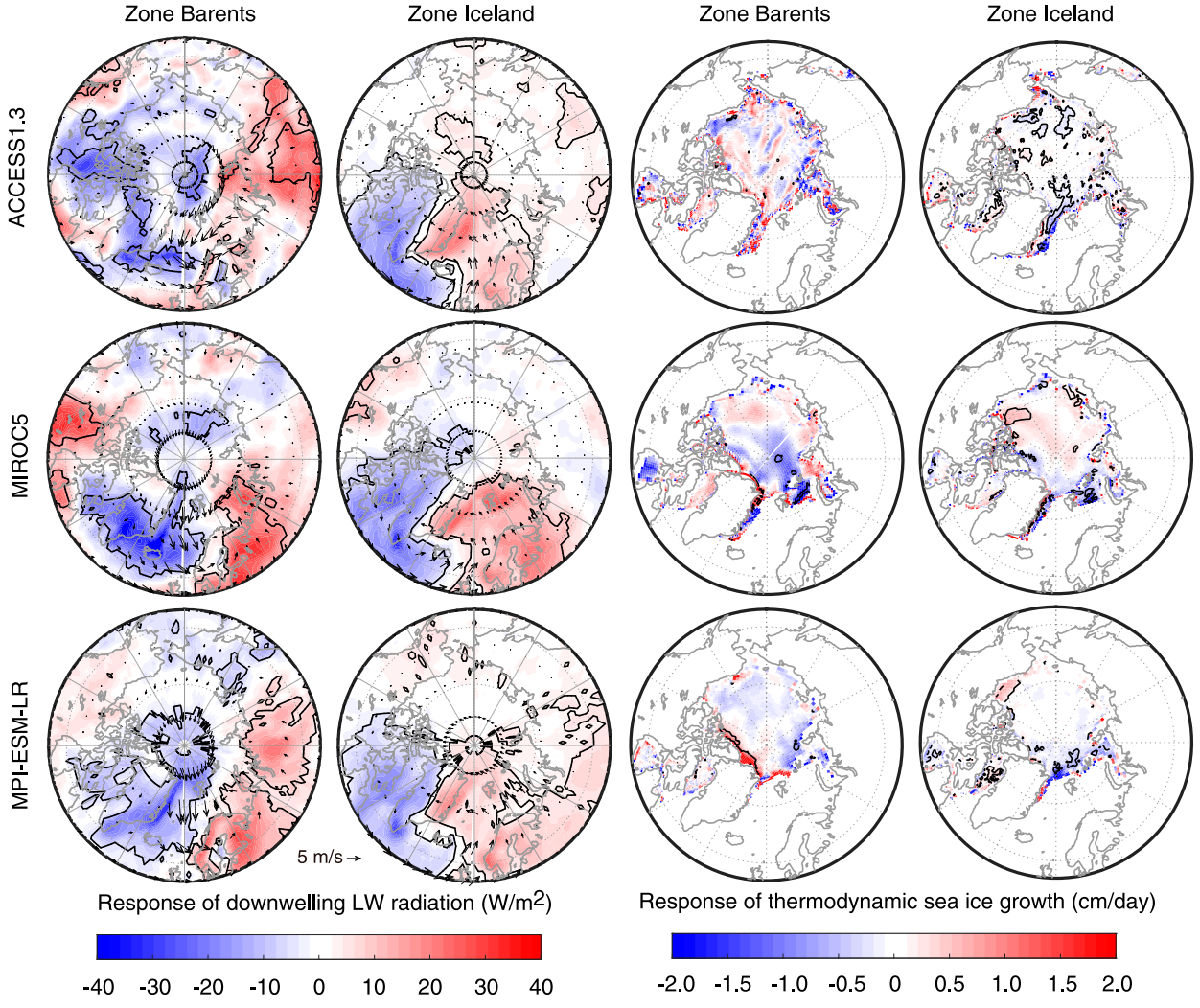

FIG. 5. As in Fig. 3, but for the projected period (2006–50) under the RCP8.5 scenario.

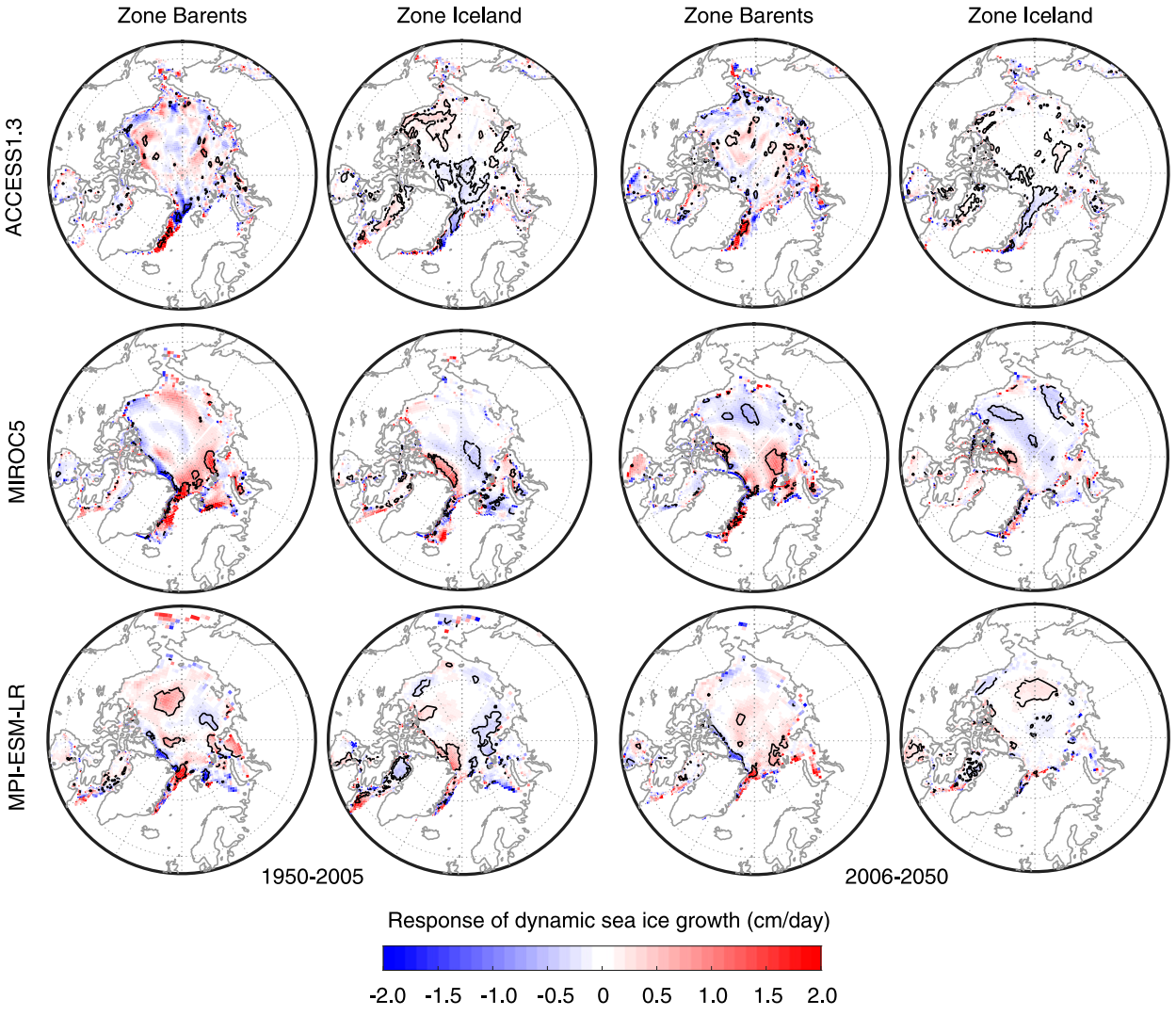

FIG. 6. Anomalies of dynamic SGR (cm day^{-1}; shaded) in response to the strong cyclones in Zone Barents and Zone Iceland in the(left) historical period (1950–2005) and (right) projected period (2006–50). Black solid lines delimit the regions in which the anomaly passes the *t* test with a 95% significance level.

opposite sign to the thermodynamic SGR response in MIROC5 and MPI-ESM-LR, indicating that the dynamic and thermodynamic SGRs offset each other. The differences in the spatial distribution of sea ice thickness and anomalous wind between models lead to the differences in the dynamic SGR responses among the models. The absolute value of the dynamic SGR response is smaller than that of the thermodynamic SGR response in all cases. Park et al. (2015) have found the stronger dynamic SGR response than thermodynamic SGR response in the first few days of the arctic moisture intrusion events. In comparison, the weaker dynamic SGR response shown in this study is not in conflict, as the cyclone identification in this study selects days with a strong cyclonic circulation pattern, which usually occurs days after the initial cyclone formation. In the RCP8.5 period, the dynamic SGR response also decreases relative to that in the historical period.

The decreased upward sensible heat flux at the surface as warm and moist air blowing into the Arctic potentially contributes to thermodynamic SGR inhibition. An examination of the sensible heat flux response shows a decreased upward sensible heat flux primarily in the sub-Arctic regions, with little influence in the central Arctic (see the figures in the supplemental material). We suggest that the sensible heat flux decrease due to atmospheric heat transport represents a partial contribution to the thermodynamic SGR inhibition over the

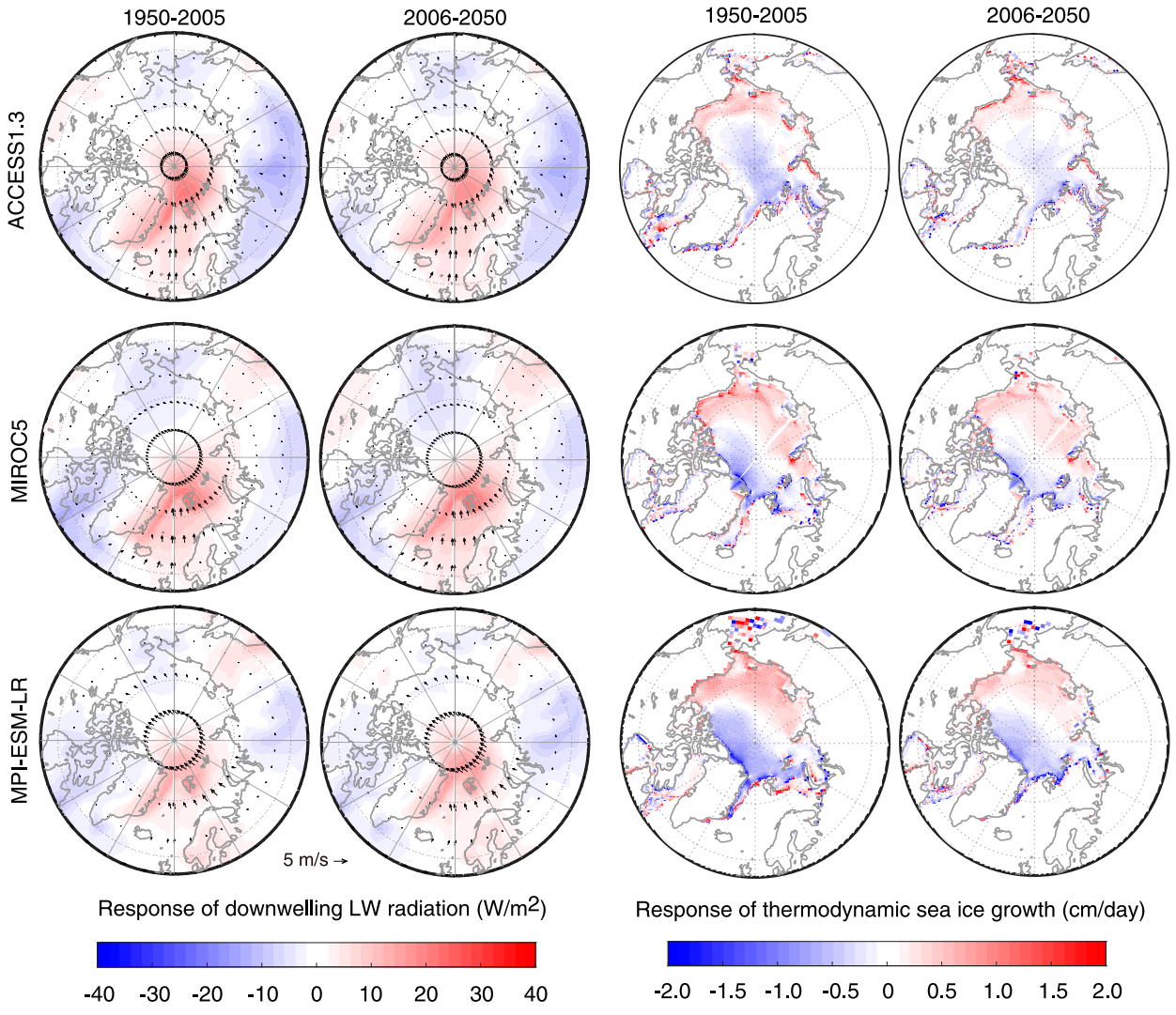

FIG. 7. (left) The map of daily DLW ($W\,m^{-2}$; shading) and wind (vectors) anomalies regressed onto the daily negative AD index in the historical and RCP8.5 periods. (right) Anomalies of thermodynamic SGR ($cm\,day^{-1}$; shading) regressed onto the daily negative AD index in the historical and the RCP8.5 periods.

Greenland and Barents Seas, while increased DLW is the dominant effect in the central Arctic Ocean to the north of Svalbard.

b. Sea ice growth response to negative AD and positive AO

The spatial distribution of daily DLW anomaly regressed onto the negative AD (the AD index multiplied by −1) is consistent with the response to the strong cyclones in Zone Iceland (Fig. 7). The regressed DLW (up to $30\,W\,m^{-2}$) and thermodynamic SGR (up to $2\,cm\,day^{-1}$) are largest in the Greenland and Barents Seas, which expands poleward. The DLW regression maps are similar between models, while the slightly different anomalous wind corresponding to the slightly different AD patterns alters the expansion direction of the thermodynamic SGR toward the central Arctic in the different models. Specifically, the regressed thermodynamic SGR inhibition in ACCESS1.3 expands directly toward the North Pole, while that in MPI-ESM-LR and MIROC5 expands toward northern Canada. For other regions, three models agree on a reduction of the thermodynamic SGR by up to $1\,cm\,day^{-1}$. The thermodynamic SGR regressed onto the negative AD has a substantially larger impact area than that associated with strong cyclones, as the negative AD corresponds to the large-scale circulation pattern and wind anomaly. We speculate that a combination of the strong Icelandic low cyclonic circulation and a negative AD in the large-scale circulation pattern would further enhance DLW

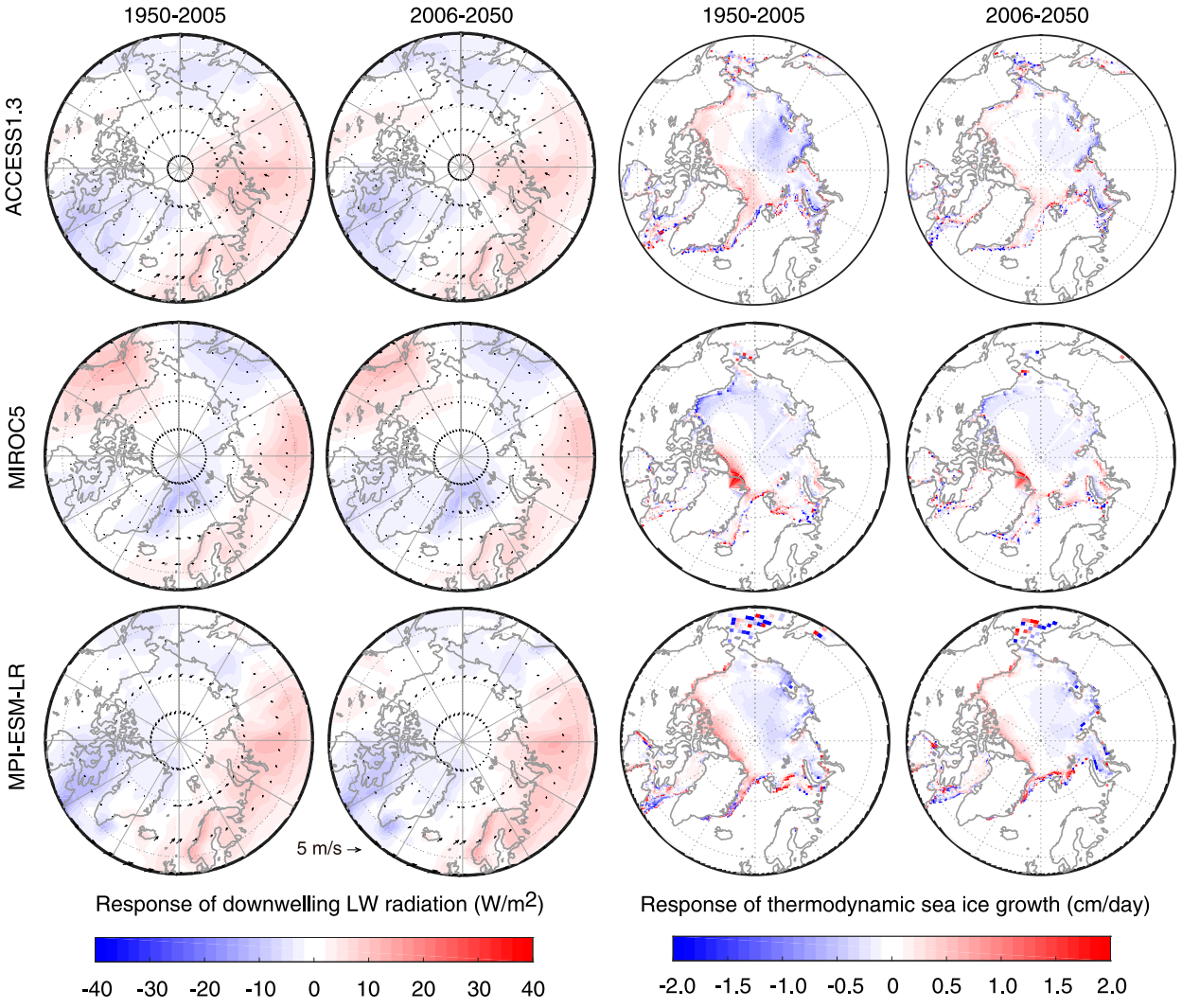

FIG. 8. As in Fig. 7, but for the regression of the daily positive AO index.

and thermodynamic SGR responses in the central Arctic.

The magnitude of the thermodynamic SGR anomaly regressed onto the negative AD is also noticeably weaker with nearly unchanged DLW regression in the RCP8.5 period than in the historical period (Fig. 7). In ACCESS1.3, for example, the thermodynamic SGR inhibition in the RCP8.5 period is at least 0.5 cm day^{-1} less than that in the historical period, and the impact area also shrinks. Similar decreases are also present in MIROC5 and MPI-ESM-LR, with about 30%–60% reductions in magnitude with smaller impact regions.

The DLW anomaly regressed on the positive AO shows a pattern similar to the response to the strong cyclones in Zone Barents (Fig. 8), but the smaller magnitudes of the DLW regression correspond to weaker (0.5 cm day^{-1}) thermodynamic SGR inhibition. The thermodynamic SGR regressed on the positive AO is also at least 50% weaker in magnitude compared to that regressed on the negative AD. The spatial patterns of DLW and thermodynamic SGR anomalies generally match that a majority of the regions with positive DLW anomalies are with negative thermodynamic SGR anomalies. Exceptions are found over the coastal regions of the Laptev Sea in MIROC5 and to the north of Bering Strait in MPI-ESM-LR, for which the negative anomalies of both the DLW and thermodynamic SGR are very small. We suggest that the negative AD is more important than the positive AO in atmospheric heat transport from the Atlantic to the central Arctic. Alexeev et al. (2017) have also argued that the process of atmospheric heat import by Atlantic cyclones does

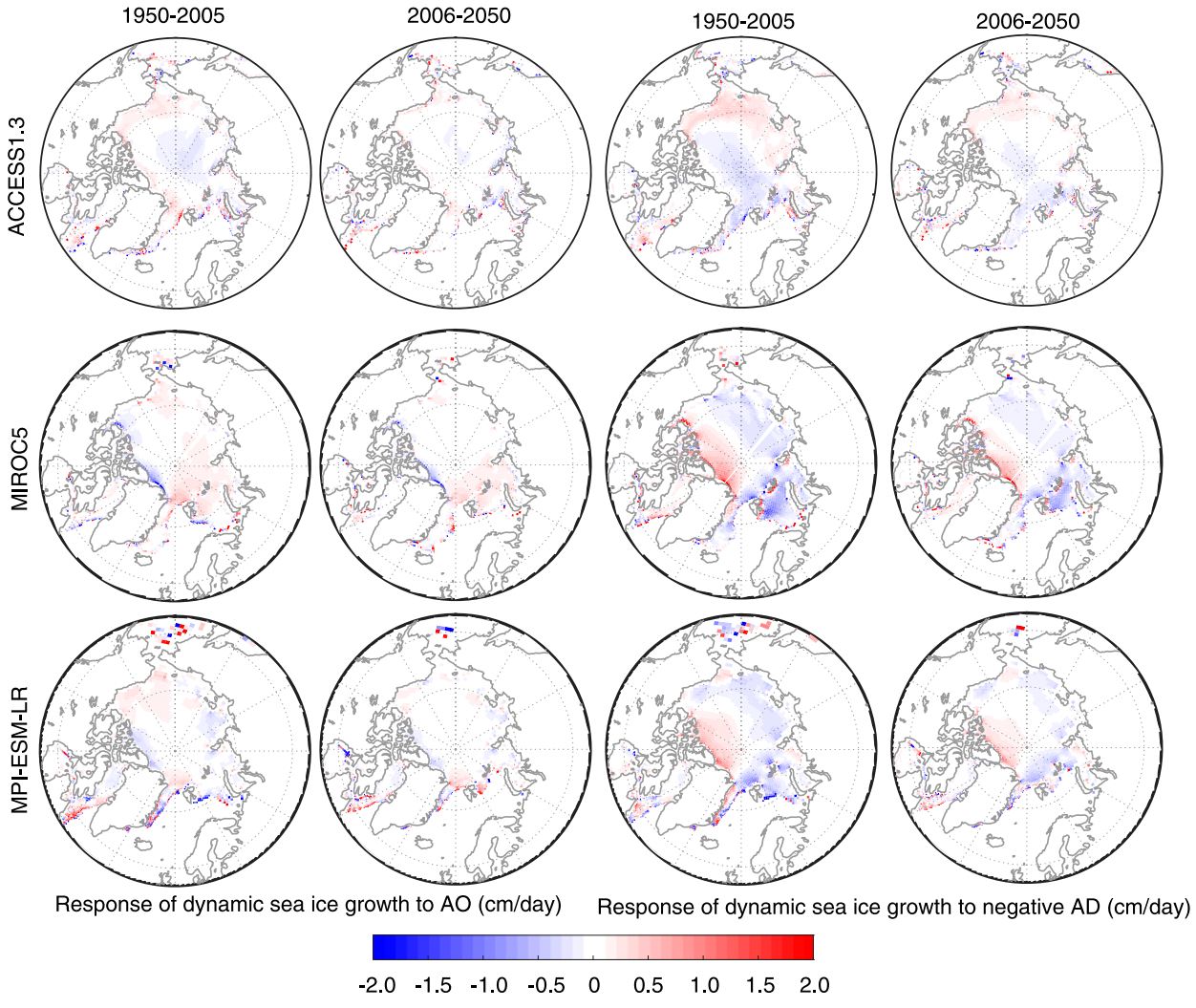

FIG. 9. Anomalies of dynamic SGR (cm day^{-1}; shaded) regressed onto (left) positive AO and (right) negative AD in the historical period (1950–2005) and projected period (2006–50).

not link directly to the AO–NAO pattern (see figure showing the composite PSL anomaly of the cyclones in the supplemental material). In the RCP8.5 period, the dampened sensitivity of thermodynamic SGR responses to the AO keeps being apparent.

Both the positive AO and negative AD are associated with the dynamic SGR, which is substantially weaker than the thermodynamic SGR on the daily scale (Fig. 9). The absolute value of regressed dynamic SGR is over 50% weaker than the regressed thermodynamic SGR for all three models. Like in the composite analysis in terms of strong cyclones, the regressed dynamic SGR in ACCESS1.3 has the same sign as that of the regressed thermodynamic SGR, while for the other models the regressed dynamic and thermodynamic SGRs have opposite signs. In the RCP8.5 period, the dynamic SGR response is weaker in all three models.

c. *Impact of a warmer Arctic on sea ice growth*

The results described in the above sections consistently show a dampened sensitivity of SGR in response to different types of atmospheric forcing in the RCP8.5 period. Statistics over the polar cap show that the 5-month (NDJFM) total sea ice growth has an increasing trend over the RCP8.5 period in all three models (Fig. 10a), leading to higher sea ice production in the warmer Arctic. Meanwhile, the standard deviation for daily SGR during the five winter months decreases, meaning that daily variability in SGR is smaller in the RCP8.5 period (Fig. 10b).

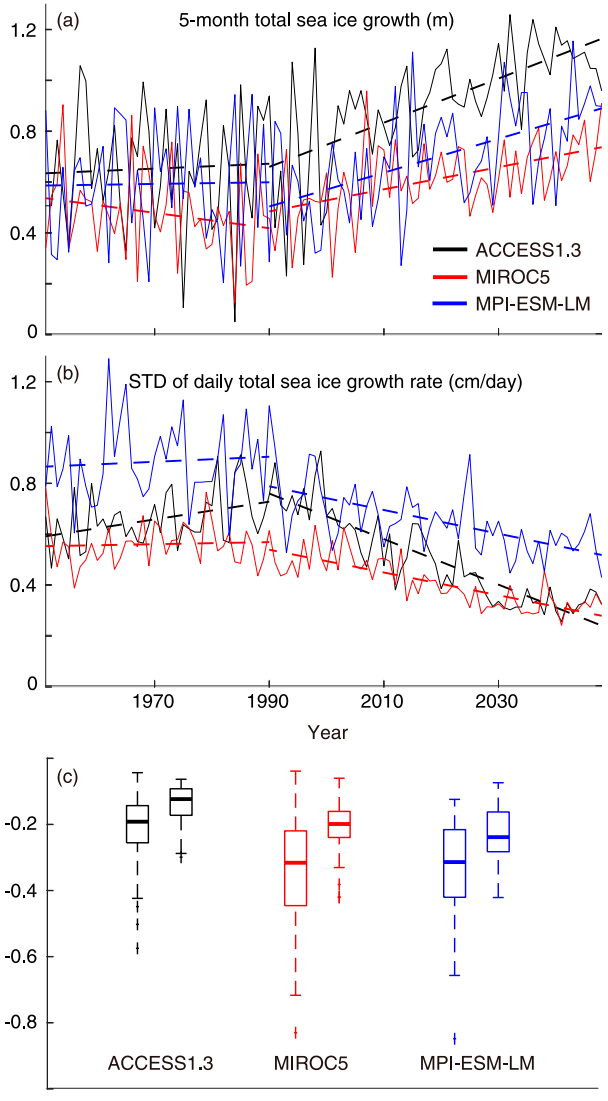

FIG. 10. Time series of (a) the total growth of sea ice and (b) the standard deviation of the daily sea ice growth rate in the 5-month period in each year in the three chosen models. Dashed lines visualize the trends. (c) Boxplot showing the statistics of negative AD–contributed sea ice growth inhibition in the historical period (left plot of each model) and the RCP8.5 period (right plot of each model).

Focusing on the negative AD, we quantify its inhibition of sea ice growth thermodynamically each winter over the polar cap by the following formula:

$$C = \sum_{i=1}^{n} (R \times \mathrm{AD}_i), \tag{2}$$

where R is the regression coefficient between the daily anomaly of thermodynamic SGR and the negative AD index (shown in Fig. 7), and AD_i is the ith of n negative AD index in the 5-month period. A negative AD reduces sea ice growth by up to 0.7 m at maximum from November to March each year in the historical period, with the average between 0.2 and 0.4 m (Fig. 10c). In the RCP8.5 period, the three models show that the AD-contributed sea ice growth inhibition decreases by at least 0.1 m, with up to a 60% decrease in interannual variability.

In winter when the atmospheric temperature is below freezing, the sea ice acts as an insulation layer inhibiting growth from its bottom, which is why thinner sea ice cover typically results in less insulation and higher winter sea ice production. Based on the empirical formula from Anderson (1961), we derive sea ice growth rate as a monotonically decreasing function of the base state sea ice thickness as a verification of the higher sea ice production with the thinner sea ice cover (see Fig. S20a in the online supplemental material). For more complex sea ice models, the CCSM3 has modeled 0.2–0.4 m more sea ice production under a doubled-CO_2 scenario (Bitz et al. 2006), comparable to the CMIP5 simulations in this study. In addition, thinner sea ice grows faster than thicker ice, so the spatial heterogeneity of sea ice thickness is expected to decrease as Arctic sea ice thickness decreases as the climate warms. Assuming the unchanged sea ice velocity, the less-varying sea ice thickness results in a smaller ice divergence flux and, in turn, a smaller dynamic SGR change in response to the strong cyclones and large-scale circulations. (See the online supplemental material for the change in the gradient of sea ice thickness.)

The numerical implementation of the thermodynamically forced sea ice growth-rate change in the CICE4 model helps to further diagnose the physics of dampened thermodynamic SGR response in the RCP8.5 period (Hunke et al. 2010). CICE4 serves as the sea ice component in ACCESS1.3 (Uotila and O'Farrell 2010), and it is probably the best-documented sea ice model among the sea ice modeling systems in CMIP5. In CICE4, the governing equation for the thermodynamic sea ice growing/melting is as follows:

$$q_{\mathrm{bot}}\delta h = (F_{\mathrm{cb}} - F_{\mathrm{bot}})\Delta t, \tag{3}$$

where in the case of sea ice growth q_{bot} is the enthalpy of the newly grown sea ice layer at the bottom, which is approximately a constant with definite freezing temperature and salinity of sea ice; δh is the change in sea ice thickness within Δt; and F_{cb} and F_{bot} are, respectively, the conductive heat flux and the net downward heat flux from ice to ocean. In the condition of extra downward energy flux ΔF_{N-1} from the overlying sea ice layer or from the atmosphere, the change ΔF_{cb} is dependent on the specific heat c_i and the thickness h_N of the Nth layer:

$$\Delta F_{\mathrm{cb}} = \frac{K_{iN+1}}{\Delta h_i}\frac{\Delta F_{N-1}}{c_i \rho_i h_N}, \tag{4}$$

in which K_{iN+1} is the thermal conductivity of the newly grown sea ice layer (beneath the Nth layer, at the bottom) with the growth rate of Δh_i ($\mathrm{m\,s^{-1}}$). The newly grown layer is the only layer that is in contact with seawater, and the temperature of which is consistently at the freezing point of seawater. The specific heat c_i is a function of sea ice temperature T (°C) and salinity S (psu):

$$c_i(T,S) = c_0 + \frac{L_0 \mu S}{T^2}, \tag{5}$$

in which c_0 and L_0 are, respectively, the specific heat and latent heat of fusion of the fresh sea ice at 0°C, and μ is a salinity parameter. Note that c_i monotonically increases with sea ice temperature.

Assuming a maximum sea ice salinity, the schematic diagram of ice growth from the bottom in response to every extra $1\,\mathrm{W\,m^{-2}}$ of downward radiation flux is derived from the above equations. In response to the same strength of extra heat flux acting on a certain thickness of sea ice, the change in SGR is a monotonous decreasing function of sea ice temperature (see Fig. S20b). In this way, we prove the reduced sensitivity of the thermodynamic SGR response in the RCP8.5 period from a physical point of view.

4. Discussion

The SGR responses to examined in this study suggests a substantially (>50%) stronger thermodynamic SGR response than dynamic SGR response on a daily scale associated with both the positive AO and negative AD. Note that what the SGR responses are associated with is a strong daily AO–AD (one standard deviation) pattern (Figs. 7 and 8). Compared to the previous study that ice drift contributes a majority of sea ice thickness change on the seasonal scale during positive AO winters (Park et al. 2018), this study complements that for a short period, the thermodynamic forcing is likely to outweigh the dynamic forcing in inhibiting sea ice growth if with a strong AO-like circulation pattern. In addition, the daily negative AD is the greater contributing factor than the positive AO in thermodynamically inhibiting daily sea ice growth, even though AO is the dominant climatic variability mode over the Arctic. It verifies our model ranking approach that prioritizes models' performance in reproducing AD in winter. In agreement with Park et al. (2015), positive DLW anomalies in all three selected models in this study can also influence the central Arctic for up to 2 weeks (or even more) in response both to the strong storms in Zone Iceland and the negative AD. Correspondingly, the thermodynamic forcing outweighs ice flux divergence in changing SGR throughout the whole period. Figure 11, as an example of the MIROC5 model, shows the anomalous DLW, as well as the accumulated SGR anomalies (both dynamic and thermodynamic) in response to strong cyclones in Zone Iceland. The SGR responses integrate from 8 days before each strong cyclone events. More figures showing a similar feature in the other two models, as well as the full methodology of integrating SGR responses, are included in the online supplemental material.

In idealized circumstances, a positive DLW anomaly should be associated with a negative thermodynamic SGR anomaly. However, comparing the spatial distributions between the anomalies of DLW and the corresponding thermodynamic SGR shows regions with inconsistent results, mostly in the Arctic coastal regions of Alaska and Siberia (Figs. 3, 5, 7, and 8). Similar inconsistency has also been found in GFDL CM3 (Park et al. 2015). We suggest that the inconsistency originates from the open-water ice formation. Open-water ice formation is more efficient than the growing of existing ice in the sea ice models because of its different physical mechanism (Hunke et al. 2010; Watanabe et al. 2010; Wetzel et al. 2010). The grid-mean SGR could still increase under the condition with heat and moisture import just because new ice can rapidly form in the open-water area when the ocean temperature is below freezing, thereby explaining the inconsistency mentioned above. In addition, we attribute the majority of the favored/inhibited open-water ice formation in our study area to the parameterized sea ice ridging processes, even though sea ice divergence can also change the area of open water and thus change the rate of new ice formation. The sea ice ridging, in this case, includes all kinds of mechanical redistribution processes including ridging, rafting, and opening/closing of leads that change sea ice concentration while keeping sea ice volume unchanged for each grid point. The change in the open-water area by sea ice ridging in this way favors or inhibits open-water ice formation during the next model time step. More detailed analyses of the surface energy budget and sea ice concentration in the online supplemental material stress why we attribute the majority of the inconsistency between the responses of DLW and thermodynamic SGR to sea ice ridging.

Both the sea ice ridging and open-water ice formation involve subgrid sea ice thickness variability, making it impossible for us to trace back the magnitude from the publicly available model output. This study calculates

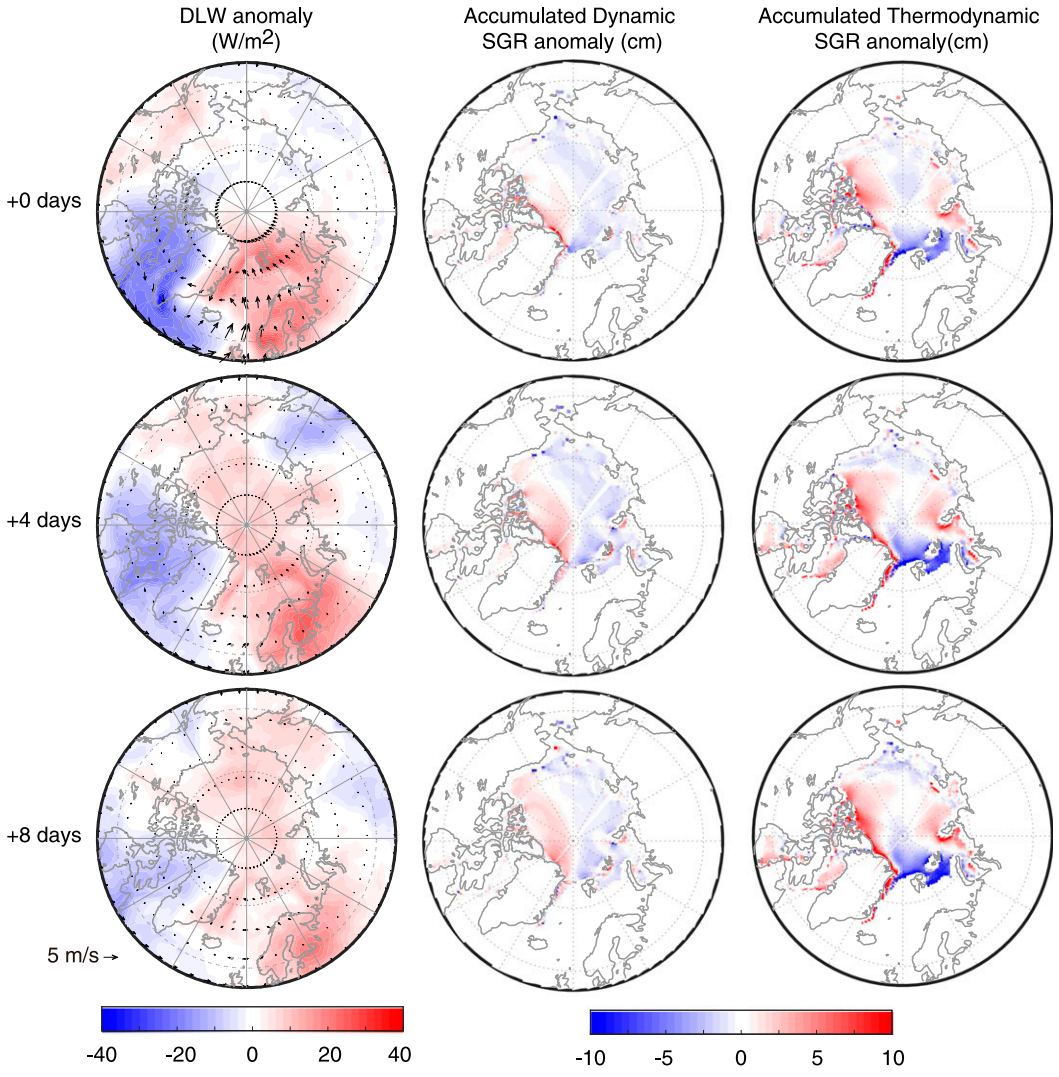

FIG. 11. (left) Anomalous DLW and the accumulated (center) dynamic and (right) thermodynamic SGR anomalies in response to strong cyclones in Zone Iceland with the lag time of (top) 0, (middle) +4, and (bottom) +8 days. Maps are made based on the data in the historical period (1950–2005) for the MIROC5 model. The accumulation of SGR responses is from 8 days before each strong cyclone event.

the thermodynamic SGR by subtracting the dynamic SGR from the total SGR, therefore involving the SGR change due to open-water ice formation as a bias in the thermodynamic SGR. The numerical implementation of ridging in these three models involves a fraction of the thinnest sea ice (15% for CICE4 and MIROC5), and sea ice ridging is more active between thinner than thicker sea ice bodies (Bitz et al. 2001; Hunke et al. 2010). During the growing season (November–April), most CICE4-simulated ridging happens along the Arctic coastal regions to the north of Alaska and Siberia, and along the ice edge on the Atlantic side (Hunke 2010). We, therefore, argue that for this study the bias of SGR response due to the neglected ridging process is small in the central Arctic (polar cap). Furthermore, excluding all grid points with the sea ice concentration less than 90% or thickness less than 0.1 m from the analysis eliminates some high-bias area along the ice edge on the Atlantic side. The remaining high-bias regions due to ridging are along the Arctic coast of Eurasia and Alaska, in which we found the most inconsistency between the anomalies of DLW and thermodynamic SGR.

CMIP5 models differ in their formulations of sea ice physics and in the response of sea ice to a warming climate (Massonnet et al. 2012). This study verifies that slight differences between models in the anomalous wind and spatial distribution of sea ice thickness can result in a substantial diversity in dynamic SGR

responses. Compared to the results in Park et al. (2018) based on GFDL CM3, ACCESS1.3 presents a similar AO-driven dynamic SGR change pattern, while MIROC5 and MPI-ESM-LR present more or less the opposite patterns spatially. This result is consistent with that in Boland et al. (2017) that the ensemble of all CMIP5 models shows a weak linkage between Arctic sea ice decline and AO. It is apparent that further studies are necessary on how and why CMIP5 models agree or disagree with each other in modeling Arctic sea ice variability in response to atmospheric circulation patterns.

The three models in this study, as well as all other CMIP5 models, differ from each other in the simulated frequency and intensity of cyclones in the Nordic seas. CMIP5 models typically underestimate the frequency and intensity of cyclones in the Norwegian Sea, and they have systematic biases in modeling the frequency and intensity of North Atlantic cyclones (Zappa et al. 2013). However, these biases do not invalidate our conclusions, as all three models demonstrate a plausible physical relationship between the atmospheric forcing and sea ice growth inhibition. High-frequency observations on sea ice thickness and atmospheric variables would help evaluate the disagreement between models. As the number of available CMIP6 products keeps growing, a similar analysis on CMIP6 model products could be interesting for the same topic assuming their numerical implementations for both the atmosphere and sea ice are more advanced than the CMIP5 models (Eyring et al. 2016).

In the RCP8.5 period, strong cyclones in Zone Iceland result in slightly smaller DLW increases over the central Arctic relative to the historical simulation. For ACCESS1.3 and MPI-ESM-LR, on the other hand, strong cyclones in Zone Iceland result in a slight increase in positive DLW anomalies over western Siberia and/or the Kara and Laptev Seas. Zappa et al. (2013) have found that in the twenty-first century, the CMIP5-modeled high-level (250-hPa) zonal wind speed is stronger over a strip-shaped region along the North Sea, the Baltic Sea, and western Siberia. Such a wind speed increase implies a change in the jet stream pathways and storm track locations that could favor extra heat and moisture transporting to western Siberia and its Arctic coastal region, which is consistent with our results in this study. We, therefore, speculate that strong cyclones in Zone Barents in the future could transport moisture and heat from the Atlantic with a higher efficiency, which impacts the regional climate and inhibits sea ice growth in the Barents, Kara, and Laptev Seas. On the other hand, the decrease in the frequency of cyclones for both zones can possibly make the wintertime Atlantic cyclone a less important contributing factor in affecting sea ice growth and Arctic warming in the future.

5. Conclusions

This study explores daily Arctic sea ice growth under the impact of winter cyclones in the Nordic Seas and large-scale atmospheric circulation patterns. We select ACCESS1.3, MIROC5, and MPI-ESM-LR from 30 CMIP5 models because of their superiority in reproducing the winter AD in the historical period (1950–2005) and data availability. A cyclone identification method enables the selection of strong cyclones in two separate regions in the Nordic seas. The total sea ice growth rate (SGR) change is considered as the sum of the growth rates due to ice drift (dynamic forcing) and thermodynamic forcing, respectively.

Both strong cyclones and large-scale circulation patterns can import atmospheric heat and moisture transports into the central Arctic, resulting in a positive anomaly of downward longwave radiation (DLW) that thermodynamically inhibits wintertime sea ice growth. Both strong cyclones in Zone Iceland and the negative AD can thermodynamically inhibit SGR in the Greenland and Barents Seas, and the regions with inhibition are extended into the central Arctic by the anomalous wind. Both strong cyclones in Zone Barents and the positive AO inhibit the thermodynamic SGR mostly along the Arctic coast of Siberia. The AO and AD as large-scale circulation patterns lead to a wider range of thermodynamic SGR inhibition than strong Nordic seas cyclones do. Because the negative AD causes stronger thermodynamic SGR inhibition in the central Arctic than the positive AO, we consider the AD as the more important mode of climatic variability in thermodynamically inhibiting wintertime sea ice growth. On the daily scale, the thermodynamic SGR change consistently exceeds the dynamic SGR change in response to strong cyclonic circulation and large-scale circulation patterns over the Arctic, including the AO and AD.

The three CMIP5 models in this study agree on a dampened sensitivity of both dynamic and thermodynamic SGR changes in response to strong cyclones and large-scale circulation patterns in the RCP8.5 future projection period. As the Arctic warms, thinner sea ice makes the insulation effect weaker, favoring sea ice growth. The smaller and less spatially variable sea ice thickness field decreases ice flux divergence, therefore decreasing the dynamic SGR response. Meanwhile, a warmer sea ice temperature increases the specific heat of sea ice, weakening thermodynamic SGR change in response to the same atmospheric heat input from

above. We suggest that the short-term SGR change due to daily-scale atmospheric forcing, including the anomalous wind pattern and enhanced downward longwave radiation from the atmosphere, will play a less important role in determining sea ice extent and thickness in the warmer Arctic.

Acknowledgments. This publication is the result in part of research sponsored by the Cooperative Institute for Alaska Research with funds from the National Oceanic and Atmospheric Administration (NOAA) under Cooperative Agreement NA13OAR4320056 with the University of Alaska. V.A. was supported by the Interdisciplinary Research for Arctic Coastal Environments (InteRFACE) project through the Department of Energy, Office of Science, Biological and Environmental Research Program's Regional and Global Model Analysis program and by NOAA project NA18OAR4590417. J.W. was supported by the National Science Foundation Grant ARC-1602720, by NOAA Grant NA17OAR4310160, and by the Office of Naval Research Grant N000141812216. We thank Nate Bauer for valuable comments on manuscript writing and for doing proofreading.

REFERENCES

Alexeev, V. A., J. E. Walsh, V. V. Ivanov, V. A. Semenov, and A. V. Smirnov, 2017: Warming in the Nordic Seas, North Atlantic storms and thinning Arctic sea ice. *Environ. Res. Lett.*, **12**, 084011, https://doi.org/10.1088/1748-9326/AA7A1D.

Anderson, D. L., 1961: Growth rate of sea ice. *J. Glaciol.*, **3**, 1170–1172, https://doi.org/10.1017/S0022143000017676.

Bitz, C. M., M. M. Holland, A. J. Weaver, and M. Eby, 2001: Simulating the ice-thickness distribution in a coupled climate model. *J. Geophys. Res.*, **106**, 2441–2463, https://doi.org/10.1029/1999JC000113.

——, J. C. Fyfe, and G. M. Flato, 2002: Sea ice response to wind forcing from AMIP models. *J. Climate*, **15**, 522–536, https://doi.org/ 10.1175/1520-0442(2002)015,0522:SIRTWF.2.0.CO;2.

——, P. R. Gent, R. A. Woodgate, M. M. Holland, and R. Lindsay, 2006: The influence of sea ice on ocean heat uptake in response to increasing CO_2. *J. Climate*, **19**, 2437–2450, https://doi.org/10.1175/JCLI3756.1.

Boisvert, L. N., A. A. Petty, and J. C. Stroeve, 2016: The impact of the extreme winter 2015/16 Arctic cyclone on the Barents–Kara Seas. *Mon. Wea. Rev.*, **144**, 4279–4287, https://doi.org/10.1175/MWR-D-16-0234.1.

Boland, E. J. D., T. J. Bracegirdle, and E. F. Shuckburgh, 2017: Assessment of sea ice–atmosphere links in CMIP5 models. *Climate Dyn.*, **49**, 683–702, https://doi.org/10.1007/s00382-016-3367-1.

Cai, L., V. A. Alexeev, J. E. Walsh, and U. S. Bhatt, 2018: Patterns, impacts, and future projections of summer variability in the Arctic from CMIP5 models. *J. Climate*, **31**, 9815–9833, https://doi.org/10.1175/JCLI-D-18-0119.1.

Deser, C., 2000: On the teleconnectivity of the ''Arctic Oscillation.'' *Geophys. Res. Lett.*, **27**, 779–782, https://doi.org/10.1029/1999GL010945.

Eyring, V., S. Bony, G. A. Meehl, C. A. Senior, B. Stevens, R. J. Stouffer, and K. E. Taylor, 2016: Overview of the Coupled Model Intercomparison Project Phase 6 (CMIP6) experimental design and organization. *Geosci. Model Dev.*, **9**, 1937–1958, https://doi.org/10.5194/gmd-9-1937-2016.

Gong, T., and D. Luo, 2017: Ural blocking as an amplifier of the Arctic sea ice decline in winter. *J. Climate*, **30**, 2639–2654, https://doi.org/10.1175/JCLI-D-16-0548.1.

Gulev, S. K., O. Zolina, and S. Grigoriev, 2001: Extratropical cyclone variability in the Northern Hemisphere winter from the NCEP/NCAR reanalysis data. *Climate Dyn.*, **17**, 795–809, https://doi.org/10.1007/s003820000145.

Hunke, E. C., 2010: Thickness sensitivities in the CICE sea ice model. *Ocean Modell.*, **34**, 137–149, https://doi.org/10.1016/j.ocemod.2010.05.004.

——, W. H. Lipscomb, A. K. Turner, N. Jeffery, and S. Elliott, 2010: CICE: The Los Alamos Sea Ice Model documentation and software user's manual version 4.1. Rep. LA-CC-06-012, Los Alamos National Laboratory T-3 Fluid Dynamics Group, 76 pp., https://csdms.colorado.edu/w/images/CICE_documentation_and_software_user%27s_manual.pdf.

Kistler, R., and Coauthors, 2001: The NCEP–NCAR 50-year Reanalysis: Monthly means CD-ROM and documentation. *Bull. Amer. Meteor. Soc.*, **82**, 247–267, https://doi.org/10.1175/1520-0477(2001)082<0247:TNNYRM>2.3.CO;2.

Kwok, R., and D. A. Rothrock, 2009: Decline in Arctic sea ice thickness from submarine and ICESat records: 1958–2008. *Geophys. Res. Lett.*, **36**, L15501, https://doi.org/10.1029/2009GL039035.

Lindsay, R., and A. Schweiger, 2015: Arctic sea ice thickness loss determined using subsurface, aircraft, and satellite observations. *Cryosphere*, **9**, 269–283, https://doi.org/10.5194/tc-9-269-2015.

Maslanik, J. A., C. Fowler, J. Stroeve, S. Drobot, J. Zwally, D. Yi, and W. Emery, 2007: A younger, thinner Arctic ice cover: Increased potential for rapid, extensive sea-ice loss. *Geophys. Res. Lett.*, **34**, L24501, https://doi.org/10.1029/2007GL032043.

Massonnet, F., T. Fichefet, H. Goosse, C. M. Bitz, G. Philippon-Berthier, M. M. Holland, and P. Y. Barriat, 2012: Constraining projections of summer Arctic sea ice. *Cryosphere*, **6**, 1383–1394, https://doi.org/10.5194/tc-6-1383-2012.

Maykut, G. A., 1978: Energy exchange over young sea ice in the central Arctic. *J. Geophys. Res.*, **83**, 3646–3658, https://doi.org/10.1029/JC083iC07p03646.

Mizuta, R., 2012: Intensification of extratropical cyclones associated with the polar jet change in the CMIP5 global warming projections. *Geophys. Res. Lett.*, **39**, L19707, https://doi.org/10.1029/2012GL053032.

NSIDC, 2018: Arctic winter warms up to a low summer ice season. National Snow and Ice Data Center, accessed 2 November 2019, https://nsidc.org/arcticseaicenews/2018/05/arctic-winter-warms-up-to-a-low-summer-ice-season/.

Park, H.-S., S. Lee, S.-W. Son, S. B. Feldstein, and Y. Kosaka, 2015: The impact of poleward moisture and sensible heat flux on Arctic winter sea ice variability. *J. Climate*, **28**, 5030–5040, https://doi.org/10.1175/JCLI-D-15-0074.1.

——, A. L. Stewart, and J.-H. Son, 2018: Dynamic and thermodynamic impacts of the winter Arctic Oscillation on summer sea ice extent. *J. Climate*, **31**, 1483–1497, https://doi.org/10.1175/JCLI-D-17-0067.1.

Phillips, A. S., C. Deser, and J. Fasullo, 2014: Evaluating modes of variability in climate models, *Eos Trans. Amer. Geophys. Union*, **95**, 453, https://doi.org/10.1002/2014EO490002.

Rigor, I. G., J. M. Wallace, and R. L. Colony, 2002: Response of sea ice to the Arctic Oscillation. *J. Climate*, **15**, 2648–2663, https://doi.org/10.1175/1520-0442(2002)015<2648:ROSITT>2.0.CO;2.

Rogers, J. C., 1997: North Atlantic storm track variability and its association to the North Atlantic Oscillation and climate variability of northern Europe. *J. Climate*, **10**, 1635–1647, https://doi.org/10.1175/1520-0442(1997)010<1635:NASTVA>2.0.CO;2.

Rudeva, I., and S. K. Gulev, 2011: Composite analysis of North Atlantic extratropical cyclones in NCEP–NCAR reanalysis data. *Mon. Wea. Rev.*, **139**, 1419–1446, https://doi.org/10.1175/2010MWR3294.1.

Serreze, M. C., and R. G. Barry, 1988: Synoptic activity in the Arctic basin, 1979–85. *J. Climate*, **1**, 1276–1295, https://doi.org/10.1175/1520-0442(1988)001<1276:SAITAB>2.0.CO;2.

——, and J. Stroeve, 2015: Arctic sea ice trends, variability and implications for seasonal ice forecasting. *Philos. Trans. Roy. Soc.*, **373A**, 20140159, https://doi.org/10.1098/rsta.2014.0159.

——, F. Carse, R. G. Barry, and J. C. Rogers, 1997: Icelandic low cyclone activity: Climatological features, linkages with the NAO, and relationships with recent changes in the Northern Hemisphere circulation. *J. Climate*, **10**, 453–464, https://doi.org/10.1175/1520-0442(1997)010<0453:ILCACF>2.0.CO;2.

——, A. P. Barrett, A. G. Slater, M. Steele, J. Zhang, and K. E. Trenberth, 2007a: The large-scale energy budget of the Arctic. *J. Geophys. Res.*, **112**, D11122, https://doi.org/10.1029/2006JD008230.

——, M. M. Holland, and J. Stroeve, 2007b: Perspectives on the Arctic's shrinking sea-ice cover. *Science*, **315**, 1533–1536, https://doi.org/10.1126/science.1139426.

Stroeve, J., M. Serreze, S. Drobot, S. Gearheard, M. Holland, J. Maslanik, W. Meier, and T. Scambos, 2008: Arctic sea ice extent plummets in 2007. *Eos, Trans. Amer. Geophys. Union*, **89**, 13, https://doi.org/10.1029/2008EO020001.

——, V. Kattsov, A. Barrett, M. Serreze, T. Pavlova, M. Holland, and W. N. Meier, 2012: Trends in Arctic sea ice extent from CMIP5, CMIP3 and observations. *Geophys. Res. Lett.*, **39**, L16502, https://doi.org/10.1029/2012GL052676.

——, A. Barrett, M. Serreze, and A. Schweiger, 2014: Using records from submarine, aircraft and satellites to evaluate climate model simulations of Arctic sea ice thickness. *Cryosphere*, **8**, 1839–1854, https://doi.org/10.5194/tc-8-1839-2014.

Taylor, K. E., R. J. Stouffer, and G. A. Meehl, 2012: An overview of CMIP5 and the experiment design. *Bull. Amer. Meteor. Soc.*, **93**, 485–498, https://doi.org/10.1175/BAMS-D-11-00094.1.

Thompson, D. W., and J. M. Wallace, 1998: The Arctic Oscillation signature in the wintertime geopotential height and temperature fields. *Geophys. Res. Lett.*, **25**, 1297–1300, https://doi.org/10.1029/98GL00950.

Tschudi, M., J. Stroeve, and J. Stewart, 2016: Relating the age of Arctic sea ice to its thickness, as measured during NASA's ICESat and IceBridge campaigns. *Remote Sens.*, **8**, 457, https://doi.org/10.3390/RS8060457.

Tsukernik, M., C. Deser, M. Alexander, and R. Tomas, 2010: Atmospheric forcing of Fram Strait sea ice export: A closer look. *Climate Dyn.*, **35**, 1349–1360, https://doi.org/10.1007/s00382-009-0647-z.

Uotila, P., and S. O'Farrell, 2010: Sea ice in the ACCESS model. CAWCR Tech. Rep. 033, 27–33, https://www.cawcr.gov.au/technical-reports/CTR_033.pdf.

Wadhams, P., and N. R. Davis, 2000: Further evidence of ice thinning in the Arctic Ocean. *Geophys. Res. Lett.*, **27**, 3973–3975, https://doi.org/10.1029/2000GL011802.

Wang, M., and J. E. Overland, 2012: A sea ice free summer Arctic within 30 years: An update from CMIP5 models. *Geophys. Res. Lett.*, **39**, L18501, https://doi.org/10.1029/2012GL052868.

Watanabe, M., and Coauthors, 2010: Improved climate simulation by MIROC5: Mean states, variability, and climate sensitivity. *J. Climate*, **23**, 6312–6335, https://doi.org/10.1175/2010JCLI3679.1.

Wei, J., X. Zhang, and Z. Wang, 2019: Impacts of extratropical storm tracks on Arctic sea ice export through Fram Strait. *Climate Dyn.*, **52**, 2235–2246, https://doi.org/10.1007/s00382-018-4254-8.

Wetzel, P., H. Haak, J. Jungclaus, and E. Maier-Reimer, 2010: The Max-Planck-Institute global ocean/sea ice model with orthogonal curvilinear coordinates. *Ocean Modell.*, **5**, 91–127, https://doi.org/10.1016/S1463-5003(02)00015-X.

Woods, C., and R. Caballero, 2016: The role of moist intrusions in winter Arctic warming and sea ice decline. *J. Climate*, **29**, 4473–4485, https://doi.org/10.1175/JCLI-D-15-0773.1.

——, ——, and G. Svensson, 2013: Large-scale circulation associated with moisture intrusions into the Arctic during winter. *Geophys. Res. Lett.*, **40**, 4717–4721, https://doi.org/10.1002/grl.50912.

——, ——, and ——, 2017: Representation of Arctic moist intrusions in CMIP5 models and implications for winter climate biases. *J. Climate*, **30**, 4083–4102, https://doi.org/10.1175/JCLI-D-16-0710.1.

Yang, W., and G. Magnusdottir, 2018: Year-to-year variability in Arctic minimum sea ice extent and its preconditions in observations and the CESM large ensemble simulations. *Sci. Rep.*, **8**, 9070, https://doi.org/10.1038/s41598-018-27149-y.

Zappa, G., L. C. Shaffrey, K. I. Hodges, P. G. Sansom, and D. B. Stephenson, 2013: A multimodel assessment of future projections of North Atlantic and European extratropical cyclones in the CMIP5 climate models. *J. Climate*, **26**, 5846–5862, https://doi.org/10.1175/JCLI-D-12-00573.1.

Zhang, X., J. E. Walsh, J. Zhang, U. S. Bhatt, and M. Ikeda, 2004: Climatology and interannual variability of Arctic cyclone activity: 1948–2002. *J. Climate*, **17**, 2300–2317, https://doi.org/10.1175/1520-0442(2004)017<2300:CAIVOA>2.0.CO;2.